

# The *Hubble* Missing Globular Cluster Survey

## II. Survey membership tools and kinematic analysis of NGC 6749

L. Rosignoli<sup>1,2,\*</sup>, M. Libralato<sup>3</sup>, R. Pascale<sup>1</sup>, D. Massari<sup>1</sup>, E. Dalessandro<sup>1</sup>, E. Ceccarelli<sup>1,2</sup>,  
H. Baumgardt<sup>4</sup>, M. Bellazzini<sup>1</sup>, A. Bellini<sup>5</sup>, F. Aguado-Agelet<sup>6,7</sup>, S. Cassisi<sup>8,9</sup>, M. Monelli<sup>8,10</sup>,  
A. Mucciarelli<sup>2,1</sup>, E. Pancino<sup>11</sup>, M. Salaris<sup>12,8</sup>, E. Dodd<sup>13</sup>, F. R. Ferraro<sup>2</sup>, and B. Lanzoni<sup>2</sup>

<sup>1</sup> INAF – Astrophysics and Space Science Observatory of Bologna, Via Gobetti 93/3, 40129 Bologna, Italy

<sup>2</sup> Department of Physics and Astronomy, University of Bologna, Via Gobetti 93/2, 40129 Bologna, Italy

<sup>3</sup> INAF, Osservatorio Astronomico di Padova, Vicolo dell'Osservatorio 5, Padova 35122, Italy

<sup>4</sup> School of Mathematics and Physics, University of Queensland, Brisbane, Qld 4072, Australia

<sup>5</sup> Space Telescope Science Institute, 3700 San Martin Drive, Baltimore, MD 21218, USA

<sup>6</sup> atlantTic, Universidade de Vigo, Escola de Enxeñaría de Telecomunicación, 36310 Vigo, Spain

<sup>7</sup> Universidad de La Laguna, Avda. Astrofísico Fco. Sánchez, 38205 La Laguna, Tenerife, Spain

<sup>8</sup> INAF – Osservatorio Astronomico di Abruzzo, Via M. Maggini, 64100 Teramo, Italy

<sup>9</sup> INFN – Sezione di Pisa, Università di Pisa, Largo Pontecorvo 3, 56127 Pisa, Italy

<sup>10</sup> INAF – Osservatorio Astronomico di Roma, Via Frascati 33, 00078 Monte Porzio Catone, Roma, Italy

<sup>11</sup> INAF – Osservatorio Astrofisico di Arcetri, Largo E. Fermi 5, 50125 Firenze, Italy

<sup>12</sup> Astrophysics Research Institute, Liverpool John Moores University, 146 Brownlow Hill, Liverpool L3 5RF, UK

<sup>13</sup> Institute for Computational Cosmology & Centre for Extragalactic Astronomy, Department of Physics, Durham University, South Road, Durham DH1 3LE, UK

Received 1 December 2025 / Accepted 27 January 2026

### ABSTRACT

The *Hubble* Missing Globular Cluster Survey has secured high-quality astro-photometric data in two bands for 34 clusters never observed with *HST*. When combined with *Gaia* astrometry, this dataset enables the investigation of the bulk motion and the internal kinematics of these poorly studied clusters to an unprecedented level of detail. Focusing on the case of NGC 6749, we show that the quality of the combined *Gaia*-*HST* proper motions is sufficient to accurately assess the cluster stellar membership, determine its absolute proper motion with a precision superior to *Gaia*, and to investigate its kinematic profile for the first time. Proper motions were determined using the public code GAIHUB, which for NGC 6749 combined datasets separated in time by ~8 years. The resulting measurements improve the precision of *Gaia* proper motions by a factor of 10 at the faint end and enabled us to recover the proper motion for 662 stars for which *Gaia* was only able to measure the positions. These proper motions efficiently decontaminate the color-magnitude diagram of NGC 6749 and made it possible to compare the efficacy of a method of statistical decontamination that only relies on the photometric information extracted from the *HST* parallel fields. Finally, using the sample of best-measured proper motions, we determined the velocity dispersion and anisotropy profiles of NGC 6749, which reveal an isotropic behavior in the inner cluster regions and a slight radial anisotropy outside 1.5 half-light radii. The proper motions and the code for statistically decontaminating the cluster's color-magnitude diagram are made available as public products of the survey.

**Key words.** methods: data analysis – astrometry – proper motions – stars: kinematics and dynamics – globular clusters: individual: NGC6749

### 1. Introduction

Globular clusters (GCs) are exceptional laboratories for understanding fundamental processes of galaxy formation and evolution (Searle & Zinn 1978). The system of the Milky Way (MW) GCs is no exception in this sense, as its chemical (see e.g., Recio-Blanco 2018; Horta et al. 2020; Monty et al. 2024; Ceccarelli et al. 2024), dynamical (e.g., Massari et al. 2019; Callingham et al. 2022; Chen & Gnedin 2024), and chronological (e.g., De Angeli et al. 2005; Marín-Franch et al. 2009; Dotter et al. 2010; Leaman et al. 2013; Massari et al. 2023) properties allow us to investigate the history of our Galaxy in detail.

Historically, the most fundamental advancements in the study of the system of the MW GCs came from observational campaigns of the *Hubble Space Telescope* (*HST*). The primary examples of these were the ACS Survey of Galactic Globular Clusters (Sarajedini et al. 2007), and the HST UV Legacy Survey of Galactic Globular Clusters (Piotto et al. 2015), which have shaped modern GC science. The latest example is the *Hubble* Missing Globular Cluster Survey (MGCS; HST Treasury Program GO-17435, PI: Massari), a campaign that has just been completed and that aims to provide homogeneous two-band photometry and astrometry for 34 GCs that have not been observed before with *HST*. The characteristics of the survey, the targets, and first results have been presented in Massari et al. (2025, Paper I, hereafter). There the authors showed that the high photometric precision achieved by the survey in the optical and near-IR

\* Corresponding author: [luca.rosignoli@inaf.it](mailto:luca.rosignoli@inaf.it)

bands enabled the determination of the age of two GCs with subgigayear precision. Paper I found that one of the two targets, 2MASS-GC01 (the highest-extincted GC currently known), might be the youngest GC known to date, even though its age of  $\sim 7$  Gyr is so young as to question its nature as a genuine GC.

While the astro-photometric catalogs of all the 34 observed targets will be made publicly available with a forthcoming publication (Libralato et al., in prep.), this paper focuses on one cluster, namely NGC 6749, and describes its analysis by means of two techniques that are both crucial to achieve the objectives of the survey.

The first part of the investigation relies on measurements of the proper motions (PMs) for the stars in common in the *HST* MGCS and *Gaia* DR3 data (Gaia Collaboration 2023). PM-based kinematic analyses of GCs have flourished in the last decade through *HST* and *Gaia*. This astrometric Renaissance has greatly improved our understanding of GCs by clearly highlighting their kinematic complexity (Bianchini et al. 2018; Sollima et al. 2019; Vasiliev & Baumgardt 2021; Libralato et al. 2022; Watkins et al. 2022; Häberle et al. 2024; Dalessandro et al. 2024). Nevertheless, kinematic information is not always available for all GCs with *HST* or *Gaia* alone because of technical limitations such as crowding, extinction, distance (for *Gaia*), or simply the lack of sufficient multi-epoch data (for *HST*). The combination of *HST* and *Gaia*, however, has shown that it is possible to bypass some of these limitations and obtain PMs for the subsample of stars common to both catalogs (see e.g., Massari et al. 2018, 2020; del Pino et al. 2022; Bennet et al. 2024; Libralato et al. 2024). This opens new possibilities of studying additional systems that were rarely studied so far.

While the *HST-Gaia* duo provides a powerful new tool, this tool is not without its own limitations. Some of the goals of the MGCS survey, such as the determination of age, mass function, and binary fraction, require a clean sample of cluster stars spanning a wide range of magnitude and masses along the main sequence (MS). However, our *HST* images can observe objects that are fainter by 5–6 magnitudes than the *Gaia* limit. Consequently, relying on *Gaia-HST* (hereafter, *GH*) PMs alone would unavoidably lead to the loss of a significant fraction of objects along the faint MS of our target clusters. For this reason, we devised an additional analysis based on the statistical decontamination of the color–magnitude diagram (CMD), taking advantage of the simultaneous *HST* observations in the core and in an external field.

In this paper, we show the application of these two techniques to the case of NGC 6749, an in situ disk GC (Massari et al. 2019, eDR3 edition) located at a distance of 7.6 kpc (Baumgardt & Vasiliev 2021). It is a relatively massive GC with a half-mass relaxation time of  $\sim 2.5$  Gyr (Baumgardt & Vasiliev 2021). Given the size of this GC (half-light radius of  $66''$  Harris (1996), 2010 edition), we were able to map the kinematics of this cluster out to about two half-light radii with a single *HST* field in the core.

In Sect. 2 we present the dataset together with photometric calibration (Sect. 2.1) and the PM estimation (Sect. 2.2). Sect. 3 describes the two methods we used to infer membership probabilities of each star. One method uses *GH* PMs (Sect. 3.1), and the other focuses on the statistical approach (Sect. 3.2). In Sect. 4, we validate the model we used to study the PMs first with a mock catalog and then by comparing our results with the literature (Sect. 4.1). After the validation, we used the *GH* PMs to perform the radial kinematic analysis of NGC 6749 (Sect. 4.2), and we derived the physical properties through an *N*-body simulation comparison in Sect. 4.3. Finally, we summarize this work in Sect. 5.

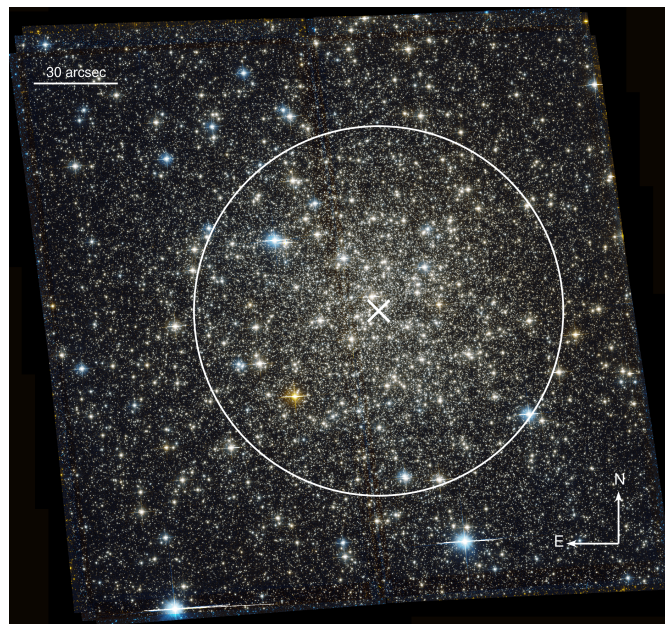


**Fig. 1.** Colored image of NGC 6749 using the new *HST* (ACS/WFC) observations. The white cross shows the center of the cluster (according to Baumgardt & Vasiliev 2021), and the radius of the white circle is equal to the half-light radius.

## 2. Data reduction

We made use of the *HST* images of NGC 6749 taken within the MGCS on 2024 March 9–12. The dataset consists of four exposures ( $2 \times 699$  s,  $1 \times 337$  s, and  $1 \times 30$  s) per filter collected with the Wide Field Channel (WFC) of the Advanced Camera for Surveys (ACS) in the F606W and F814W bands on target, and of an analog set of parallel exposures with an identical setup using the Ultraviolet and Visible Instrument (UVIS) of the Wide Field Camera 3 (WFC3). The ACS/WFC data cover the central region of the cluster, as shown in Fig. 1, whereas the WFC3/UVIS parallel fields are off center by about 7 arcmin.

### 2.1. Photometry

This dataset was reduced as described in Massari et al. (2025), in accordance with the well-established prescriptions outlined in a number of papers presenting high-precision astrometry and photometry with *HST* images (Bellini et al. 2017; Nardiello et al. 2018; Libralato et al. 2018, 2022). We refer to Paper I and to the forthcoming paper by Libralato et al. for the details of the astro-photometric analysis. Briefly, the data reduction consists of two steps called first- and second-pass photometry. The first-pass photometry is used to create the initial astro-photometric catalogs, one for each *HST* image<sup>1</sup>. The positions and magnitudes in these catalogs were obtained via the software *hst1pass*<sup>2</sup> (Anderson 2022a,b), which performs an effective-point-spread-function (ePSF) fit by means of the publicly available *HST* ePSF models, appropriately fine-tuned for each image. The positions

<sup>1</sup> We made use of `_flc` exposures, i.e., dark- and bias-corrected, flat-fielded, nonresampled images that were pipeline-corrected for the charge-transfer-efficiency defects (Anderson & Ryon 2018).

<sup>2</sup> The code and its ancillary files can be found here: <https://www.stsci.edu/~jayander/HST1PASS/>

are corrected for the effect of geometric distortion using publicly available corrections<sup>3</sup>. These first-pass catalogs are used to set up the astrometric and photometric reference systems for the second-pass photometry. The second-pass photometry is obtained with proprietary software KS2 (Anderson in prep.; Bellini et al. 2017), which analyzes all input images at once (thus enhancing the detection of faint sources) and is designed to overcome crowding-related limitations typical of environments such as GCs.

## 2.2. Astrometry

The astrometric analysis of NGC 6749 focuses on the central field observed with the ACS/WFC alone. The PMs of the stars in this region are computed by means of the publicly available tool GAI AHUB (del Pino et al. 2022). GAI AHUB combines *HST* and *Gaia* data to obtain PMs with a temporal baseline longer than that of the *Gaia*-DR3 PMs. As shown, for instance, by del Pino et al. (2022) and Bennet et al. (2024), GAI AHUB delivers PMs that can be more precise by one order of magnitude than those of *Gaia* at the *Gaia* faint end and in crowded environments.

GAI AHUB relies on astro-photometric catalogs computed for each *HST* image by means of the first-pass-photometry tool `hst1pass`, which is run in the background at the beginning of the process. To ensure a self-consistent infrastructure throughout our project, we modified GAI AHUB to use our first-pass astro-photometric catalogs (Sect. 2.1) instead of producing its own.

Before computing PMs, GAI AHUB transforms *HST* positions onto the reference frame of *Gaia* via a six-parameter linear transformation (two offsets, one rotation, one change of scale, and two skew terms<sup>4</sup>). In general, the coefficients of such transformations are computed by comparing two sets of positions of the same reference stars. If these positions are taken at different epochs, these transformations would map the different alignment between the frames and the actual motion of the reference stars between the two epochs. In our case, the latter contribution would bias our frame alignment because cluster and field stars have significantly different motions. To solve for this problem, we might either select a single group of stars (e.g., cluster stars, whose velocity dispersion and coherent motion would imprint a minimum contribution in the transformations), or propagate the positions of one of the two catalogs at the epoch of the other catalog (so that all stars can be used, regardless of the population to which they belong). We chose the latter option (using the `--rewind_stars` flag) to avoid a membership selection that at this stage might bias our PMs<sup>5</sup>, and to increase statistics.

The absolute PMs from GAI AHUB of the stars in the central field of NGC 6749 present a series of systematics as a function of position, magnitude, and color. We corrected for these systematic errors by comparing our *GH* PMs with those in the *Gaia* DR3 catalog. A detailed description of the systematic corrections is provided in Appendix A.

A comparison between our *GH* and the *Gaia* PMs is shown in Fig. 2. The top panels present the vector-point diagrams (VPDs) of the PMs in the *Gaia* DR3 catalog (left panel) and our

<sup>3</sup> Can be found in <https://www.stsci.edu/~jayander/./STDGDCs/>

<sup>4</sup> Skew terms represent the deviation from orthogonality and the relative scale difference between the two axes.

<sup>5</sup> For completeness, we also tested the membership option (`--members` flag) and found a slightly worse result because the contaminating field component and the cluster stars overlap significantly, which makes the membership selection challenging.

PMs (middle and right panels). While the middle panel presents objects with a counterpart entry in the *Gaia* catalog, the right panel only includes sources without a PM in the *Gaia* catalog. The comparison of the VPDs for the same stars in our and *Gaia* panels (middle and left panels, respectively) already provides a qualitative assessment of the improvement brought by the *HST-Gaia* synergy, as the more populated clump in these diagrams (i.e., the distribution of the cluster stars) looks tighter with our PMs than with those in the *Gaia* DR3 catalog. This improvement in precision is more quantitatively shown in the two bottom panels in Fig. 2, where we compare the PM errors in each component of the motion as a function of *G* magnitude. At magnitudes fainter than  $G \approx 18.5$ , our PMs become more precise than the ones from *Gaia* by a factor of 3 and up to 10 at the very faint end, with a median value of  $\delta_\mu = 0.42$  mas/yr for *GH* and  $\delta_\mu = 1.09$  mas/yr for *Gaia*<sup>6</sup>. Furthermore, the GAI AHUB catalog contains PMs for 2634 stars compared to the 1972 from *Gaia*, incrementing by 662 the number of stars with this information. This de facto extends the astrometry to stars fainter by  $\sim 0.5$  mag than in the *Gaia* catalog.

To reject poor measurements<sup>7</sup>, we applied the following criteria (Bellini et al. 2014; Libralato et al. 2018, 2022):

$$\delta_\mu \leq 0.5 * \sigma_\mu^{\text{local}}(n), \quad (1)$$

where  $\delta_\mu$  is the PM error, and  $\sigma_\mu^{\text{local}}$  is the local velocity dispersion measured using the  $n = 20$  closest stars to each source (target excluded). Figure 3 shows the vector point diagram (VPD) and the CMD of NGC 6749. In the VPD, a tight clump of stars located at about  $(\mu_\alpha \cos \delta, \mu_\delta) = (-3, -5.5)$  mas yr<sup>-1</sup> is embedded in other sources with a broader distribution. We selected stars within a radius of 1.0 mas yr<sup>-1</sup> from the center of the tight clump (red circle) and plotted them in the CMDs (red dots in the middle panel). As expected, these are mainly cluster members (well aligned along the evolutionary sequences in the CMD), whereas the broadly distributed population in the VPD (those beyond the red circle in the left panel) comprises field stars along the line of sight of the cluster (black dots in the CMD). Zooming in around the CMD location of these stars (right panel), we can identify the cluster red giant branch (RGB) and horizontal branch (HB). In the following section, we address the problem of the cluster membership in a quantitative way using two different approaches.

## 3. Membership probability

We adopted two independent approaches to estimate the membership probability of the cluster sources detected in the MGCS images. The first approach only exploits the PM measurements, and the second approach only relies on the CMD comparison between the target and the WFC3/UVIS parallel observations. In Sections 3.1 and 3.2, we thoroughly describe each method, and in Sect. 3.3, we compare the two membership selections.

<sup>6</sup> For a magnitude below  $G \approx 18.5$ , the raw *GH* PMs are still better than those of *Gaia*. In particular, the median error value for *GH* is  $\delta_\mu = 0.04$  mas/yr compared to  $\delta_\mu = 0.22$  mas/yr for *Gaia*, but after the calibration described in Appendix A, the error increase due to the square-root summation of the initial error with the uncertainty on the correction.

<sup>7</sup> We focused on well-measured sources identified photometrically by means of a mix of percentile-based selections on the quality of the ePSF fit, magnitude rms, and stellarity index, number of images used in the flux measurement, impact of the neighbor flux, and local sky (see, e.g., Libralato et al. 2022; Massari et al. 2025, and Libralato et al., in prep.).

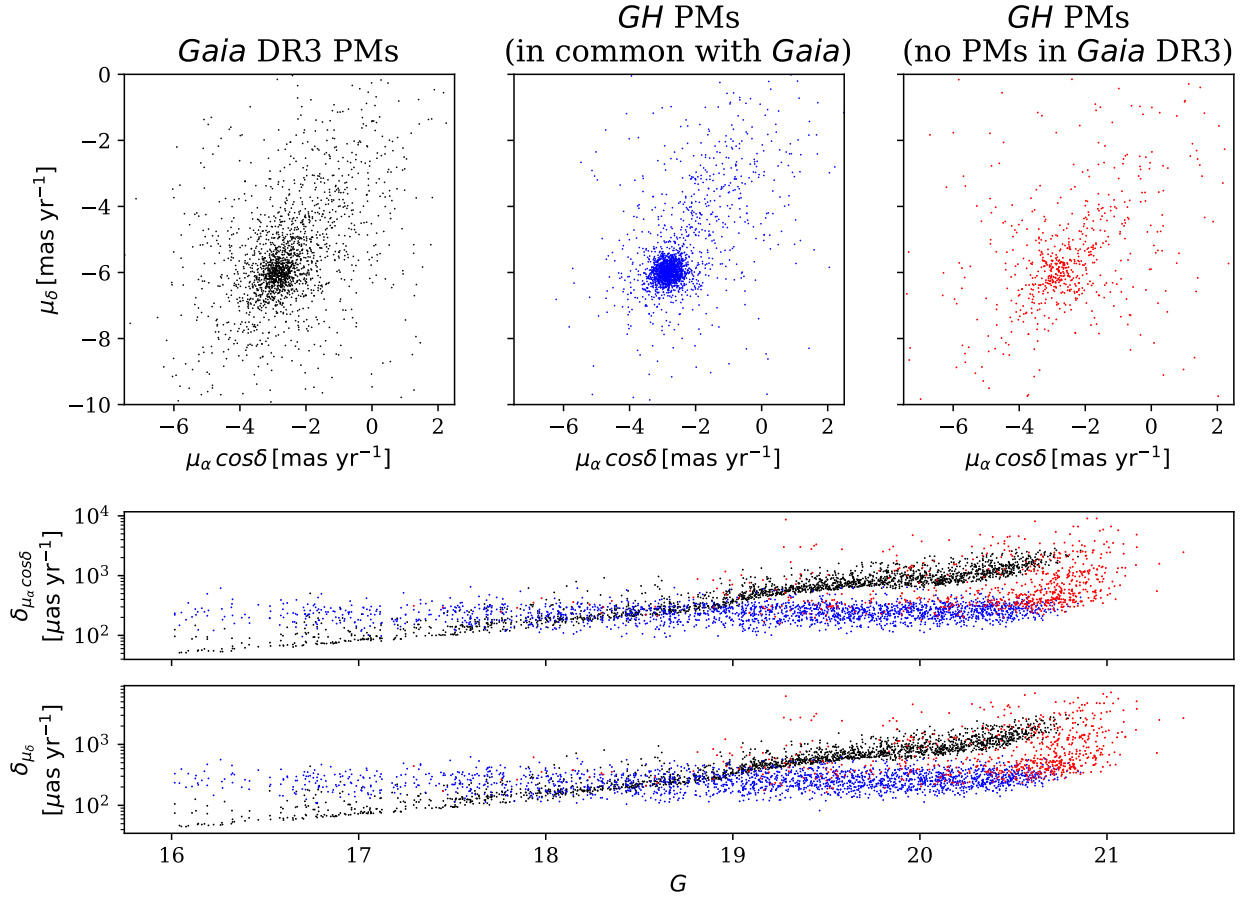


**Fig. 2.** Comparison between the *Gaia* and *GH* PMs. The top panels show the VPDs of the PMs, and the two bottom panels show the PM errors along  $\alpha \cos \delta$  and  $\delta$  as a function of *Gaia*  $G$  magnitude. The black dots refer to the *Gaia* PMs, and the blue and red dots show stars in our catalog with and without a corresponding PM in the *Gaia* catalog, respectively.

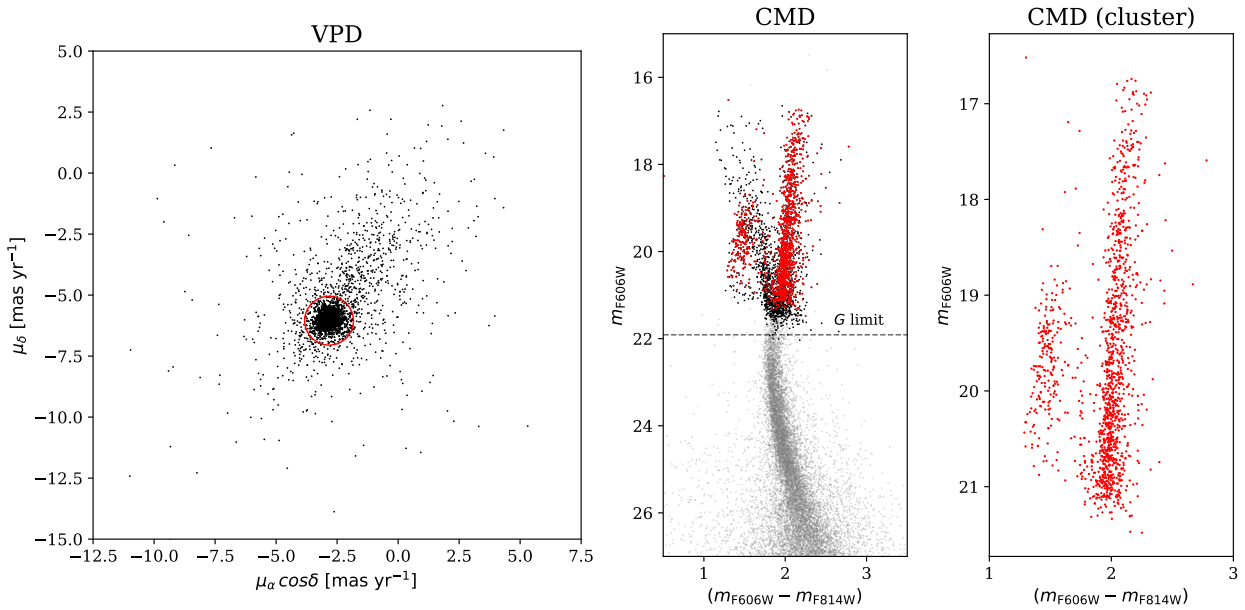


**Fig. 3.** VPD (left panel) and CMDs (middle and right panels) of NGC 6749 using the new *HST* data of the MGCS survey. The red circle with the radius of  $1 \text{ mas yr}^{-1}$  in the VPD was used to select likely cluster stars (those included within the circle). In the central CMD, the gray dots represent all stars in our *HST* photometric catalog, and the black and red dots are foreground and cluster stars, respectively, for which we have a PM measurements. The horizontal dashed line corresponds to the *Gaia* limiting magnitude. Finally, the right panel shows the location of cluster member stars in the CMD.

### 3.1. Kinematic membership

The PM distributions of a GC and the background field often overlap significantly (Bellini et al. 2014; Libralato et al. 2022). This overlap complicates a clear-cut separation between members and nonmembers, which thereby necessitates a probabilistic approach. This approach assumes that the observed sample of stellar PMs is a realization of an underlying model. In its general form, this model consists of  $n_{\text{comp}}$  components, each corresponding to a distinct stellar population with its own kinematic structure and contributing to the global PM probability distribution  $\mathcal{P}(\boldsymbol{\mu})$ ,

$$\mathcal{P}(\boldsymbol{\mu}) = \sum_{i=1}^{n_{\text{comp}}} w_i \mathcal{P}_i(\boldsymbol{\mu}). \quad (2)$$

In the equation above,  $\boldsymbol{\mu} \equiv (\mu_\alpha \cos \delta, \mu_\delta)$ ,  $\mathcal{P}_i(\boldsymbol{\mu})$  is the probability distribution of each component, and  $w_i$  represents its fractional contribution. We further required that

$$\sum_{i=1}^{n_{\text{comp}}} w_i = 1 \quad (3)$$

to ensure a proper normalization. The model parameters were determined within a fully Bayesian framework by maximizing a well-motivated likelihood function of the data. When the parameters were determined, the model provided a probabilistic framework for assigning a membership probability to each star with respect to the different components.

In our specific application, we distinguished between two Gaussian components (i.e., a Gaussian mixture model; GMM): the target GC, and a term describing the foreground contamination (FG). Therefore, the model probability distribution (2) reduces to

$$\mathcal{P}(\boldsymbol{\mu}) = w_1 G_{\text{GC}}(\boldsymbol{\mu}) + (1 - w_1) G_{\text{FG}}(\boldsymbol{\mu}), \quad (4)$$

where  $G_{\text{GC}}$  and  $G_{\text{FG}}$  describe the PM distributions of the GC and the foreground stars, respectively, and  $w_1$  sets the relative contribution of the GC over the foreground.

We modeled each component as a bivariate Gaussian,

$$G_i(\boldsymbol{\mu}) = \frac{\exp[-\frac{1}{2}(\boldsymbol{\mu} - \hat{\boldsymbol{\mu}}_i)^T \Sigma_i^{-1}(\boldsymbol{\mu} - \hat{\boldsymbol{\mu}}_i)]}{\sqrt{(2\pi)^2 \det \Sigma_i}}, \quad (5)$$

where  $\hat{\boldsymbol{\mu}}_i = (\hat{\mu}_{\alpha,i}, \hat{\mu}_{\delta,i})$ , and  $\Sigma_i$  are the center and the covariance matrix of the  $i$ th component, respectively, with  $i=\text{GC}$  or  $\text{FG}$ . The covariance matrix  $\Sigma_i$  is

$$\Sigma_i = \begin{pmatrix} \sigma_{\alpha,i}^2 & \rho_i \sigma_{\alpha,i} \sigma_{\delta,i} \\ \rho_i \sigma_{\alpha,i} \sigma_{\delta,i} & \sigma_{\delta,i}^2 \end{pmatrix}. \quad (6)$$

The model consists of the following free parameters, one per component ( $i=\text{GC}$  or  $\text{FG}$ ):

- $\hat{\boldsymbol{\mu}}_i(\alpha, \delta)$  is the center of motion of each component.
- $\sigma_i(\alpha, \delta)$  is the standard deviation of each component.
- $\rho_i$  is the correlation between the standard deviation components.
- $w_1$  is the weight of the GC Gaussian in the mixture.

This is for a total of six free parameters.

The likelihood of the model for the observed dataset is

$$\mathcal{L} = \prod_j (\mathcal{P} * \mathcal{E})(\boldsymbol{\mu}_j), \quad (7)$$

where the product extends over the stars in our sample, the asterisk represents the convolution with the error function  $\mathcal{E}$ , which is a bivariate Gaussian distribution with null mean, and the covariance is given by

$$\Sigma = \begin{pmatrix} \varepsilon^2 & 0 \\ 0 & \varepsilon^2 \end{pmatrix}. \quad (8)$$

One of the great advantages of using Gaussians when describing multiple components in a mixture model is that the convolution between each model component and the error function is still a Gaussian with a mean and covariance matrix,  $\Sigma_i^{\text{obs}}$ , given by the sums of the individual means and covariance matrices. In our specific case, the resulting covariance matrix can be written as

$$\Sigma_i^{\text{obs}} = \begin{pmatrix} (\sigma_{\alpha,i}^{\text{obs}})^2 & \rho_i^{\text{obs}} \sigma_{\alpha,i}^{\text{obs}} \sigma_{\delta,i}^{\text{obs}} \\ \rho_i^{\text{obs}} \sigma_{\alpha,i}^{\text{obs}} \sigma_{\delta,i}^{\text{obs}} & (\sigma_{\delta,i}^{\text{obs}})^2 \end{pmatrix}, \quad (9)$$

where we called

$$\sigma_i^{\text{obs}} = \sqrt{\sigma_i^2 + \varepsilon^2} \quad (10)$$

with  $\sigma_i^{\text{obs}} = (\sigma_{\alpha,i}^{\text{obs}}, \sigma_{\delta,i}^{\text{obs}})$  and

$$\rho_i^{\text{obs}} = \rho_i \frac{\sigma_{\alpha,i} \sigma_{\delta,i}}{\sigma_{\alpha,i}^{\text{obs}} \sigma_{\delta,i}^{\text{obs}}}. \quad (11)$$

In the above equations,  $i = \text{GC}$  or  $\text{FG}$ .

We determined the free model parameters using a Monte Carlo Markov chain (MCMC) method, relying on the EMCEE package (Foreman-Mackey et al. 2013). To sample the posterior and determine the model parameter confidence intervals, we ran an MCMC with 50 walkers, each evolved for 10 000 steps. We discarded the first 500 steps of each walker as burn-in and applied a thinning factor of 20, consistent with median value of the autocorrelation lengths of the free parameters, thereby ensuring a sample of effectively independent draws. The remaining steps were used to compute the distributions for the free model parameters. The median parameter values and any other derived quantity of the models were estimated as the 50th percentile of the corresponding distributions; the  $1\sigma$  credible intervals were determined using the 16th and 84th percentiles of the distributions.

We assigned a membership probability to each star in the sample in the following way. For each star  $k$ , we computed the distribution of  $p_k$ , that is, the probability of the  $k$ th star to belong to the GC. This probability is defined as

$$p_k = \frac{w_1 (G_{\text{GC}} * \mathcal{E})(\boldsymbol{\mu}_k)}{(\mathcal{P} * \mathcal{E})(\boldsymbol{\mu}_k)}. \quad (12)$$

Consistently with credible interval estimates, we took as the probability the 50th percentile of the distribution. Figure 4 shows the VPD of NGC 6749 for 2184 stars using the new *GH* PMs, together with the marginal distributions the membership probability. As an example, the number of stars with a membership probability  $p > 0.8$  is 1416.

### 3.2. Photometric membership

Even though the membership obtained from the PMs is more accurate, the kinematic information is only available for a limited number of stars. Another approach exploits the CMD to

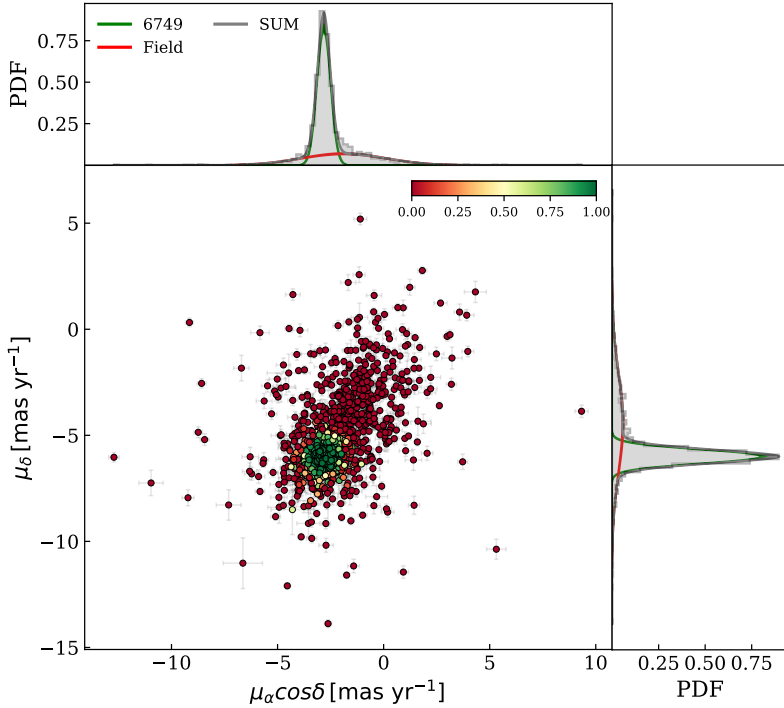


**Fig. 4.** Distribution of the NGC 6749 GH PMs. The central scatter plot shows the 2D VPD, where the points are color-coded by the membership probability obtained from the MCMC chains (color bar). The top and right histograms show the normalized marginal distributions of the PMs, together with the posterior distributions of the GMM components, the target in red, the field in blue, and their sum in gray.

statistically infer the membership. When the photometric information is used, the number of suitable stars increases drastically. In the case of NGC 6749, we calculated the membership probability for 50 097 stars. This method requires the observation of a parallel field that is close enough to the target to be representative of the contaminating stellar population, but sufficiently far away to exclude GC members. Many algorithms have been proposed over the past 20 years to determine the membership in this way (e.g., Mighell et al. 1996; Knoetig 2014; Cabrera-Ziri et al. 2016). The general idea behind these algorithms is that the CMD of the field can be statistically subtracted from the CMD of the target GC. Some approaches defined a specific metric to evaluate the space nearby each star in order to understand its likelihood of being a contaminating star (e.g. Milone et al. 2018). Other algorithms implement a statistical subtraction to retrieve the membership probability. These approaches usually divide the CMD (the target and the parallel field) space in cells. For each cell, the information from the field CMD is used to perform a statistical subtraction in the same cell of the target CMD. Some implementations use a cell with a fixed size (Bonatto & Bica 2007; Dalessandro et al. 2019), while more recent works use adaptive grids. Our approach belongs to the latter case and works as follows. We tried to preserve the spatial resolution of the target CMD as much as possible while keeping a sufficient statistics per cell to avoid shot-noise bias. The grid was created via a Voronoi tessellation that naturally follows the stellar density in the CMD. Moreover, to ensure a uniform spatial distribution of contaminating stars (as we expect from a field population), we split the statistical subtraction into radial bins that always contained the same number of contaminants (see for example Dalessandro et al. 2019). At the beginning of the process, the membership was set to 1.0 for every star, and the following steps were then made to update the membership:

1. Creation of the Voronoi grid, based on the target CMD of the stars contained in the radial bin.
2. Dilation of the Voronoi grid. By design, the Voronoi grid creates a cell for each star. If we performed the following

steps with only one star per cell, the final membership distribution would be biased by the shot noise. For this purpose, the Voronoi tessellation was diluted by merging the closest cells, starting from the smallest ones. This process was repeated until the distribution of the number of stars per cell had a median value equal to or greater than a desired threshold. We set a threshold of ten stars as the best trade-off between the loss of the grid resolution and a good statistics per cell<sup>8</sup>.

3. Count of the number of stars in the field CMD that fall in each cell,  $n_{field}$ .
4. Rescale  $n_{field}$  for the ratio of the field of view (FoV) of the parallel field ( $fov_{field}$ ) and the sky area covered by the current radial bin ( $fov_{bin}$ ),  $n_{sub} = n_{field} \cdot \frac{fov_{bin}}{fov_{field}}$ .
5. Convert  $n_{sub}$  from a decimal into integer number with the following criteria:

$$n'_{sub} = \begin{cases} \mathcal{B}([1 - n_{sub}, n_{sub}]), & \text{if } n_{sub} < 1 \\ \text{int}(n_{sub}) + \mathcal{B}([1 - \text{dig}(n_{sub}), \text{dig}(n_{sub})]), & \text{if } n_{sub} \geq 1 \end{cases}$$

where  $\text{int}(n_{sub})$  and  $\text{dig}(n_{sub})$  are the mantissa and the decimal digits, respectively, and  $\mathcal{B}$  is the Bernoulli distribution. In this way, we tried to take the decimal part of the normalized  $n_{sub}$  into account.

6. For each cell,  $n'_{sub}$  target stars were randomly subtracted. When  $n'_{sub}$  was greater than the number of target stars within the cell, then all the stars were subtracted. This step was repeated many times (1000 in our case) to further mitigate the shot noise.
7. For each star, the membership was computed as follows:

$$m_i = 1 - \frac{n_i^{sub}}{n_j^{total}}, \quad (13)$$

<sup>8</sup> The value of ten stars worked for this cluster, but this number has to be evaluated for each case, depending on the number of available stars.

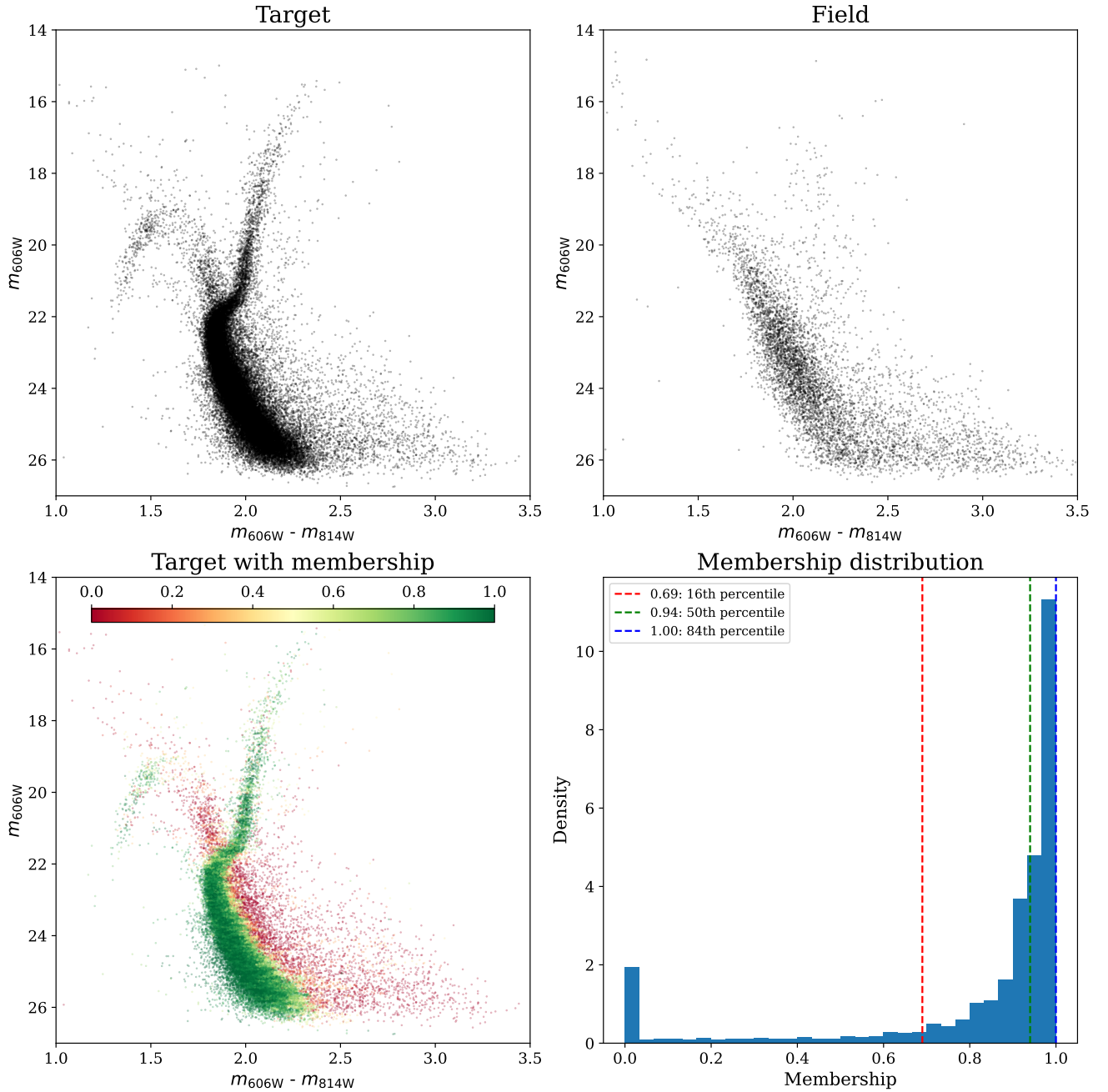


**Fig. 5.** Result of the statistical decontamination. (Top left panel) Contaminated target CMD. (Top right panel) Parallel field CMD. (Bottom left panel) Target CMD color-coded for the membership probability. (Bottom right panel) Membership probability distribution. The target CMDs were corrected for the differential reddening.

where  $n_i^{sub}$  is the number of times that the  $i$ th star was subtracted, and  $n_j^{total}$  is the total number of subtractions made in the  $j$ th cell that contains the star.

The process of statistical subtraction was combined with a differential reddening correction using the algorithm described in Milone et al. (2012). We iteratively combined the differential reddening correction and the statistical subtraction through the following algorithm:

1. The differential reddening correction of the target CMD was performed using as reference stars only those with a membership probability higher than a certain threshold (we used 90%). For the first iteration, all the stars were used because their membership probability is one.

2. We performed the statistical decontamination of the CMD using the differential reddening corrected magnitudes.
3. We iterated the two steps by updating the membership probabilities and the reddening correction.

We considered that the process reached convergence when the typical residual reddening corrections were on the order of the photometric error, which in this case was after three iterations. The result of our procedure is shown in Fig. 5. The top panels show the reddening-corrected CMDs of NGC 6749 and of its parallel field, respectively. From these, it is already evident that the overlap between the target main sequence (MS) and the field MS is quite strong, making this a challenging case for the statistical approach. The panel in the lower left corner shows the same

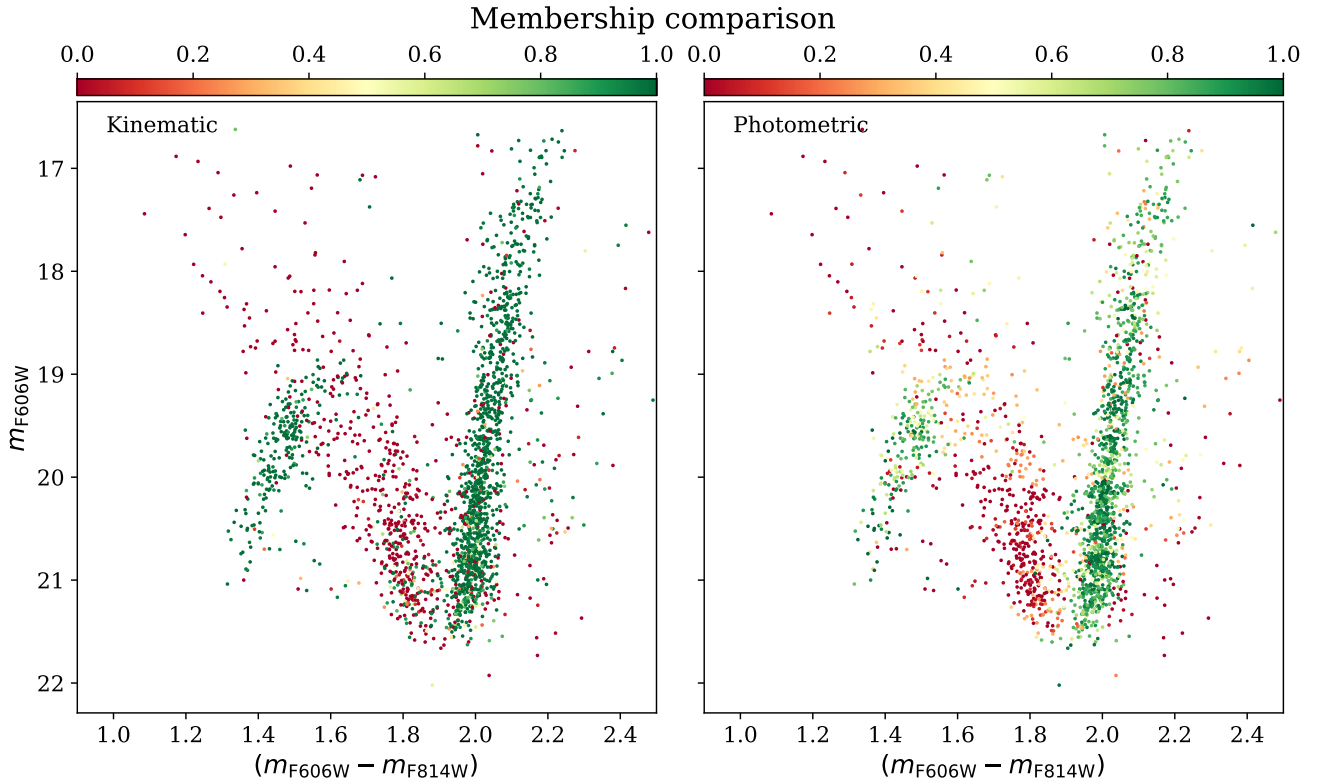


**Fig. 6.** Color-coded CMDs according to the membership probability. (*Left*) Membership calculated from the PMs. (*Right*) Membership obtained with the statistical approach.

target CMD, but color-coded based on the membership probability, which in turn is displayed in the lower right corner. The CMD of likely members appears to be very well defined, with likely contaminants populating the expected bluer and brighter sequence typically attributed to MW disk stars in the GC foreground or background. To give the same reference as for the kinematic membership in Section 3.1, the number of stars with  $p > 0.8$  is 41 838.

### 3.3. Comparison between the two methods

Using stars with both photometric and kinematic information, we directly compared the membership distributions obtained with the two methods described above. In Fig. 6 the target CMD is color-coded according to the membership probability obtained from the kinematic approach in the left panel and the photometric approach in the right panel. The two results are remarkably similar and thus demonstrate that the photometric procedure has worked successfully. For the sake of comparison, the 75% of stars with a kinematic membership  $p > 0.8$  also have a photometric membership  $p > 0.8$ . Since this method will primarily be adopted by MGCS, for GCs with different properties, it is worth discussing some of the limitations that the statistical approach has compared to the kinematic approach. First, it is limited by the number of stars in the target CMD. In particular, few stars in the target CMD means a larger Voronoi cell size, which lowers the resolution and the ability to sample small and isolated features. Second, the dilation of the Voronoi cells at the edges of features such as the MS and the giant branches merges some of the small cells and maps the feature itself with the large cells that map the almost empty space next to it. As a result, these are more likely to be oversubtracted during the process. This mimics an

erosion effect of the feature edges, where the membership probability is lower than in the inner parts. Finally, where no field signal is present in some cell (meaning that no stars are found in that cell in the field CMD), the membership is exactly one, while when the field signal dominates the target (i.e., when there are more field stars in that cell than the target stars), the membership drops to zero. However, the result shown in Figs. 5 and 6 suggests that our statistical approach is a valid method for decontaminating the entire target CMD. Therefore, we advise any user to select one method over the other depending on the needs of the specific science case of interest.

## 4. Kinematic analysis

By using the unprecedentedly precise PMs we measured and the GMM described in Section 3.1, we performed a detailed analysis of the internal kinematics of NGC 6749. First, we validated our approach in two ways: *i*) with a mock catalog with known parameters (see Section 4.1), and *ii*) with the *Gaia* DR3 PMs in the literature. After the validation, we refine in Section 4.2 the mean PM of the GC and build the first PM-dispersion radial profile for NGC 6749.

### 4.1. Validation with a mock catalog and external checks

We made a first validation of our GMM using a mock distribution of PMs, which qualitatively resembled the distribution shown in the VPD of NGC 6749, convolved with an error of  $0.5 \text{ mas yr}^{-1}$ . Table 1 summarizes the comparison between the posterior distributions of the GMM parameters using the median value as reference and the 16th and 84th as uncertainties (i.e., the  $1\sigma$  confidence range), and the parameters used to generate the

**Table 1.** Comparison between the posterior model distributions and the mock model.

Parameters	Posterior	Mock
$\mu_{\alpha} \cos \delta^{GC}$ [mas yr <sup>-1</sup> ]	$-3.03^{+0.02}_{-0.03}$	-3.00
$\mu_{\alpha} \cos \delta^{Field}$ [mas yr <sup>-1</sup> ]	$-1.68^{+0.15}_{-0.15}$	-1.75
$\mu_{\delta}^{GC}$ [mas yr <sup>-1</sup> ]	$-5.45^{+0.03}_{-0.02}$	-5.50
$\mu_{\delta}^{Field}$ [mas yr <sup>-1</sup> ]	$-4.51^{+0.15}_{-0.14}$	-4.25
$\sigma_{\alpha}^{GC}$ [mas yr <sup>-1</sup> ]	$0.19^{+0.05}_{-0.07}$	0.21
$\sigma_{\alpha}^{Field}$ [mas yr <sup>-1</sup> ]	$2.50^{+0.11}_{-0.11}$	2.50
$\sigma_{\delta}^{GC}$ [mas yr <sup>-1</sup> ]	$0.20^{+0.06}_{-0.07}$	0.21
$\sigma_{\delta}^{Field}$ [mas yr <sup>-1</sup> ]	$2.58^{+0.12}_{-0.12}$	2.50
$\rho_{\alpha\delta}^{GC}$ [ ]	$0.03^{+0.05}_{-0.05}$	0.0
$\rho_{\alpha\delta}^{Field}$ [ ]	$0.25^{+0.05}_{-0.05}$	0.3
$w_{GC}$ [ ]	$0.65^{+0.02}_{-0.02}$	0.67
$w_{Field}$ [ ]	$0.35^{+0.02}_{-0.02}$	0.33

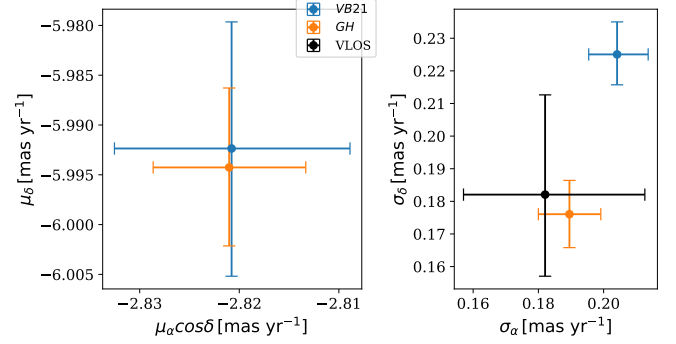
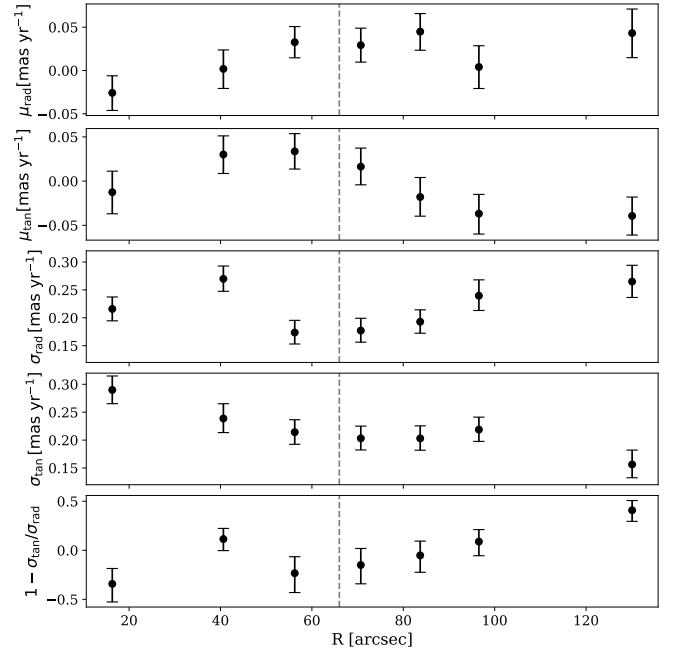
mock distribution. The posterior distributions are always consistent within  $1\sigma$  with the true input values, except for the mean motion of the cluster and the field along the declination (the  $\mu_{\delta}$  component), which are consistent with the input within  $2\sigma$ , probably because in the shape of the VPD, the  $\delta$  direction is most affected by the overlap between the cluster and the field component. However, this test shows that our GMM can successfully recover the properties of a PM distribution where the field and cluster components overlap strongly.

After the validation with the mock PMs, we tested our approach on the sample of member stars of NGC 6749 that were used to obtain the value of velocity dispersion quoted in Vasiliev & Baumgardt (2021). We remark that in this test (VB21 hereafter), we used a single-component GMM (i.e. a 2D Gaussian fit) because the sample consisted of member stars alone.

Figure 7 shows the comparison of the cluster mean motion components  $\mu_{\alpha,\delta}$  and the PM dispersions  $\sigma_{\alpha,\delta}$  of the two PM distributions. This figure shows that the  $\mu_{\alpha,\delta}$  of the cluster component is well consistent between the two cases. Our measurement provides a mean PM of  $\mu_{\alpha,\delta} = (-2.82, -5.99)$  mas yr<sup>-1</sup>, with a smaller uncertainty ( $0.008$  mas yr<sup>-1</sup>) than VB21 ( $0.012$  mas yr<sup>-1</sup>). On the other hand, we find a larger discrepancy (at the  $3\sigma$  level) in  $\sigma_{\delta}$ , with our GH PMs providing  $\sigma_{\delta} = 0.18 \pm 0.01$  mas yr<sup>-1</sup>, while for the VB21 sample, we determine  $\sigma_{\delta} = 0.23 \pm 0.01$  mas yr<sup>-1</sup>.

To understand which of the two estimates is more realistic, we compared it with the current line-of-sight velocity dispersion values available for NGC 6749<sup>9</sup>, that is,  $\sigma_{VLOS} = 6.55^{+1.10}_{-0.90}$  km/s, as measured with a combination of Gaia DR3, Apogee DR19, and published literature RVs. Under the assumption of isotropy, our GH velocity dispersion estimates of  $\sigma_{\alpha} = 6.83$  km/s and  $\sigma_{\delta} = 6.34$  km/s (assuming a distance of 7.59 kpc, Baumgardt & Vasiliev 2021) agree better than those we obtained from VB21 of  $\sigma_{\alpha} = 7.35$  km/s and  $\sigma_{\delta} = 8.11$  km/s. This is reasonable evidence that our measurements led to an improved estimate of the cluster velocity dispersion. Our more precise GH PMs probably allow for a better deconvolution of cluster and field components in the GMM and thus enable a better selection of the actual stellar members. In passing, we also provide an estimate for the kinematic distance ( $d_{kin}$ ) of NGC 6749. Under the usual assumption

<sup>9</sup> Baumgardt H., private communication.

**Fig. 7.** Comparison of the mean velocity (left) and velocity dispersion (right) components for GH (orange), and GaiaDR3-VB21 (blue). The error bars are the 16th and 84th of the posterior parameter distribution. The current line-of-sight velocity dispersion (black) is shown as reference.**Fig. 8.** Radial profiles of the mean velocity ( $\mu_{rad,tan}$ ), velocity dispersion ( $\sigma_{rad,tan}$ ), and anisotropy (calculated as  $1 - \frac{\sigma_{tan}}{\sigma_{rad}}$ ) for NGC 6749. The half-light radius (dashed gray line) is shown as reference.

of isotropy, the tangential velocity dispersion that we measured matches that along the line of sight for  $d_{kin} = 6.92 \pm 0.36$  kpc, which is consistent within  $1.2\sigma$  with the distance quoted by Baumgardt & Vasiliev (2021) of  $d = 7.59 \pm 0.22$  kpc.

#### 4.2. Kinematic analysis of NGC 6749

Based on the available large number of stars with measured PMs, we investigated the internal kinematics of NGC 6749. We divided our field into annular bins with a variable area, each containing at least 300 stars. We also decomposed our PMs from equatorial coordinates into their radial and tangential components to study features such as kinematic anisotropies and overall expansion and rotation in the plane of the sky. As we pointed out in Section 2.2, our GH PMs are more precise than Gaia's at its faint end ( $G \gtrsim 18.5$ ), while for brighter stars ( $G \lesssim 18.5$ ), Gaia is still the best option. For this reason, we decided to construct

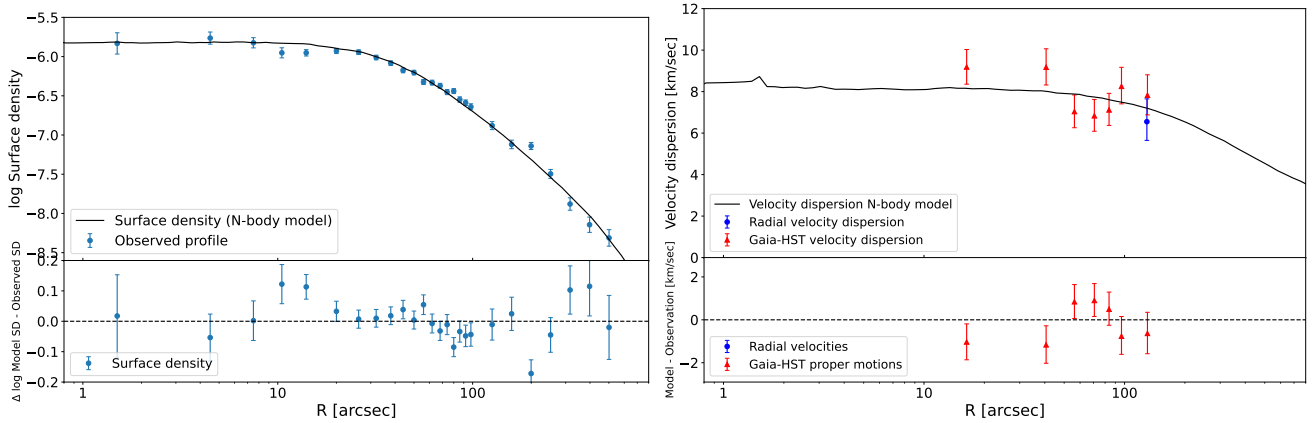


**Fig. 9.** Comparison of the surface density profile (*left*) and the velocity dispersion profile (*right*) of NGC 6749 with the best-fitting  $N$ -body model from the grid of models from Baumgardt & Hilker (2018). The model and observations agree well.

a golden sample of stars by selecting the PMs with the lowest uncertainty from either *GH* or *Gaia*. For each bin, we modeled the VPD using the GMM described in Section 3.1 by fixing the parameters of the field component to the median value of its posterior distribution, obtained using the golden sample. Figure 8 reports the radial trends of the cluster mean PM and PM dispersions along the radial and tangential directions  $\sigma_{rad,tan}$ . We also measured the ratio of the radial and tangential components of the velocity dispersion and thus obtained the anisotropy profile of NGC 6749. The trend of the mean GC motion as a function of radius can be indicative of kinematic features such as rotation or expansion or contraction. In our case, the best-fit linear trends give an angular coefficient of  $(5.0 \pm 2.2 \cdot 10^{-4}) \text{ mas yr}^{-1} \text{ arcsec}^{-1}$  in the radial direction and  $(5.0 \pm 2.9 \cdot 10^{-4}) \text{ mas yr}^{-1} \text{ arcsec}^{-1}$  in the tangential one. These numbers might indicate mild systematic motions, particularly in the radial direction, where the trend is inconsistent with zero at  $2.2\sigma$ . We also verified that, given the cluster distance,  $v_{LOS}$ <sup>10</sup>, and FoV covered by our data, any correction for perspective effects is about  $10^{-3} \text{ mas yr}^{-1}$  and is therefore negligible compared to the magnitude of the observed trends. However, given the relatively small field of view covered by our PMs, we prefer to avoid strong claims and leave this as possible evidence to be investigated further.

We detected a rather flat behavior in the radial direction of the PM dispersion profile and a decreasing trend along the tangential component. The resulting anisotropy profile shows a slightly increasing trend, with isotropy holding to a distance of about 100 arcsec, and a mild radial anisotropy at a distance larger than  $\sim 120''$ . Considering the values from Harris (1996, 2010 edition;  $37''$  and  $66''$  for core and half-light radii, respectively), our anisotropy profile agrees qualitatively with that of GCs with an intermediate dynamical age shown by Libralato et al. (2022), but its velocity dispersion radial profile is steeper than that of GCs with the same concentration index ( $c = 0.79$ ). A more detailed analysis of the structural properties of this GC based on the exquisite new *HST* data is necessary to further investigate the system.

#### 4.3. Comparison with simulations

In order to derive the physical parameters of NGC 6749 from the new velocity dispersion profile, we searched the grid of

$N$ -body simulations that produced the best match of the surface density and velocity dispersion profile of NGC 6749 from Baumgardt & Hilker (2018). In order to compare with the  $N$ -body simulations, we summed the observed radial and tangential velocity dispersions at each radius, which appeared to be justified because the velocity dispersion is close to isotropic over most of the radial range that we measured. We scaled all  $N$ -body simulations in radius to match the observed half-light radius of NGC 6749 and then interpolated in the grid of simulations to find the best-fitting  $N$ -body model. We then derived the physical parameters of NGC 6749 from the  $N$ -body simulations as described in Baumgardt & Hilker (2018). Fig. 9 shows the result of our fitting process. We obtained a good fit to the velocity dispersion and surface density of NGC 6749, and our proper motion velocity dispersion profile agrees well with the radial velocity dispersion profile for an assumed cluster distance of 7.6 kpc. We find a total cluster mass of  $M_C = (5.53 \pm 0.28) \cdot 10^5 M_\odot$ , a projected central dispersion of  $\sigma_0 = 8.0 \pm 0.64 \text{ km s}^{-1}$ , an  $M/L$  ratio of  $M/L = 3.65 \pm 0.27 M_\odot/L_\odot$ , and a half-mass radius of  $r_h = 7.1 \text{ pc}$ . This places NGC 6749 among the 10% most massive GCs in the MW.

## 5. Conclusions

As a part of the MGCS treasury program (Massari et al. 2025), we presented new *HST* observations of NGC 6749 that we used to develop new publicly available Python-based tools for the photometric-based membership determination and kinematic analysis of GCs (and GC-like objects).

By combining our MGCS *HST* observations (Massari et al. 2025) with *Gaia* DR3 using the software GAIHUB, we determined unprecedentedly precise PMs for this GC. In particular, we were able to decrease the PM error by up to one order of magnitude at the faint end ( $G > 18.5$ ), and for the first time, we determine PMs for stars that only had *Gaia* positions measured so far.

We analyzed the resulting VPD of NGC 6749 using GMM. This method comprises an inference-based approach that uses MCMC simulations to find the posterior distribution of the model parameters. Our model has the flexibility of managing an arbitrary number of Gaussian components and can fix and/or link any parameter to another. A natural product of this procedure is the probability of each star to belong to NGC 6749. We compared this kinematic membership with that stemming

<sup>10</sup> Quoted in [people.smp.uq.edu.au/HolgerBaumgardt/globular/orbits](http://people.smp.uq.edu.au/HolgerBaumgardt/globular/orbits)

from a photometric approach that combines a statistical CMD subtraction, featured with an adaptive Voronoi-based grid generation, with correction for differential reddening. This iterative approach improved the membership probability and differential reddening correction at each iteration. The comparison between the two methods is remarkably good, with the photometric algorithm ensuring an appropriate CMD decontamination even for stars that are too faint to have PM information.

Our kinematic analysis was first validated with a mock catalog and then with existing kinematic measurements, thus verifying the efficacy of our method in separating cluster and field components even in a relatively highly contaminated case. The mean motion of NGC 6749 of  $\mu_{\alpha,\delta} = (-2.82, -5.99) \pm 0.008 \text{ mas yr}^{-1}$  was determined with a precision better than *Gaia*. Given the large number of stars with a precise PM measurement, we were able to investigate the kinematic profiles of NGC 6749 for the first time. By using a golden sample of PMs that combined the best measurements from ours and *Gaia* catalogs, we built the profiles of  $\mu_{rad,tan}$ ,  $\sigma_{rad,tan}$ , and the anisotropy ( $\sigma_{tan}/\sigma_{rad}$ ). The general kinematic picture of GCs drawn by *HST* (Libralato et al. 2022) agrees overall. Finally, the comparison of our observed kinematic profile with *N*-body simulations revealed that NGC 6749 belongs to the 10% most massive GC in the Galaxy, with a total mass of  $M = (5.53 \pm 0.28) \cdot 10^5 M_{\odot}$ .

## Data availability

All the tools presented here are available at the GitHub repository [https://github.com/LR-inaf/MGCS\\_pytools.git](https://github.com/LR-inaf/MGCS_pytools.git) or at the PyPi repository <https://pypi.org/project/MGCS-pytools/>.

*Acknowledgements.* D.M., S.C., E.P. and A.M. acknowledge financial support from PRIN-MIUR-22: CHRONOS: adjusting the clock(s) to unveil the CHRONO-chemo-dynamical Structure of the Galaxy” (PI: S. Cassisi). A.M. and M.B. acknowledge support from the project “LEGO – Reconstructing the building blocks of the Galaxy by chemical tagging” (PI: A. Mucciarelli), granted by the Italian MUR through contract PRIN 2022LLP8TK\_001. M.M. acknowledges support from the Agencia Estatal de Investigación del Ministerio de Ciencia e Innovación (MCIN/AEI) under the grant “RR Lyrae stars, a lighthouse to distant galaxies and early galaxy evolution” and the European Regional Development Fun (ERDF) with reference PID2021-127042OB-I00. Co-funded by the European Union (ERC-2022-AdG, “StarDance: the non-canonical evolution of stars in clusters”, Grant Agreement 101093572, PI: E. Pancino). Views and opinions expressed are however those of the author(s) only and do not necessarily reflect those of the European Union or the European Research Council. Neither the European Union nor the granting authority can be held responsible for them. This paper is supported by the Italian Research Center on High Performance Computing Big Data and Quantum Computing (ICSC), project funded by European Union – NextGenerationEU – and National Recovery and Resilience Plan (NRRP) – Mission 4 Component 2 within the activities of Spoke 3 (Astrophysics and Cosmos Observations). This work is part of the project Cosmic-Lab at the Physics and Astronomy Department “A. Righi” of the Bologna University (<http://www.cosmic-lab.eu/Cosmic-Lab/Home.html>). Based on observations with the NASA/ESA HST, obtained at the Space Telescope Science Institute, which is operated by AURA, Inc., under NASA contract NAS 5-26555. Support for Program number GO-17435 was provided through grants from STScI under NASA contract NAS5-26555. This research made use of emcee (Foreman-Mackey et al. 2013). This work has made use of

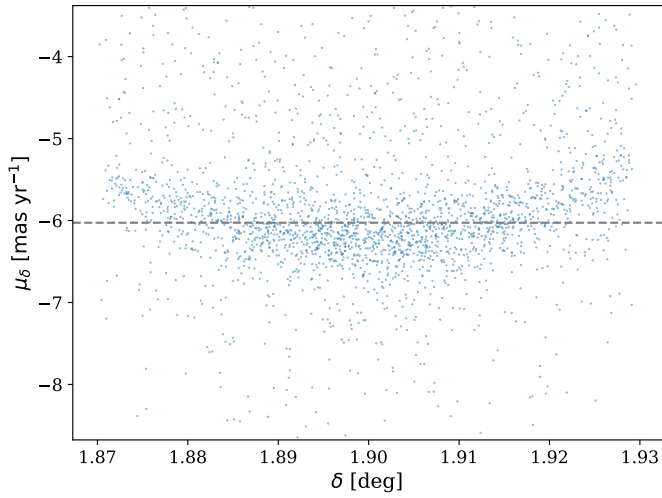
data from the European Space Agency (ESA) mission *Gaia* (<https://www.cosmos.esa.int/gaia>), processed by the *Gaia* Data Processing and Analysis Consortium (DPAC, <https://www.cosmos.esa.int/web/gaia/dpac/consortium>). Funding for the DPAC has been provided by national institutions, in particular the institutions participating in the *Gaia* Multilateral Agreement. ED acknowledges financial support from the INAF Data Analysis Research Grant (PI E. Dalessandro) of the “Bando Astrofisica Fondamentale 2024”.

## References

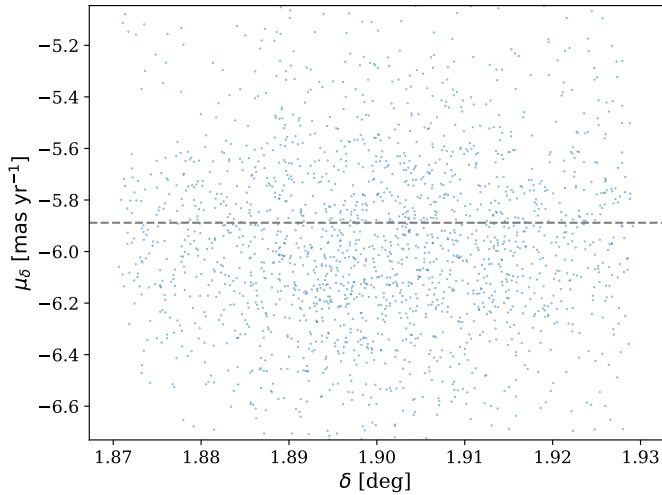
- Anderson, J. 2022a, *One-Pass HST Photometry with hstlpass*, Instrument Science Report ACS 2022-02
- Anderson, J. 2022b, *One-Pass HST Photometry with hstlpass*, Instrument Science Report WFC3 2022-5, 55
- Anderson, J., & Ryon, J. E. 2018, *Improving the Pixel-Based CTE-correction Model for ACS/WFC*, Instrument Science Report ACS 2018-04, 37
- Baumgardt, H., & Hilker, M. 2018, *MNRAS*, 478, 1520
- Baumgardt, H., & Vasiliev, E. 2021, *MNRAS*, 505, 5957
- Bellini, A., Anderson, J., van der Marel, R. P., et al. 2014, *ApJ*, 797, 115
- Bellini, A., Anderson, J., Bedin, L. R., et al. 2017, *ApJ*, 842, 6
- Bennet, P., Patel, E., Sohn, S. T., et al. 2024, *ApJ*, 971, 98
- Bianchini, P., van der Marel, R. P., del Pino, A., et al. 2018, *MNRAS*, 481, 2125
- Bonatto, C., & Bica, E. 2007, *MNRAS*, 377, 1301
- Cabrera-Ziri, I., Niederhofer, F., Bastian, N., et al. 2016, *MNRAS*, 459, 4218
- Callingham, T. M., Cautun, M., Deason, A. J., et al. 2022, *MNRAS*, 513, 4107
- Ceccarelli, E., Mucciarelli, A., Massari, D., Bellazzini, M., & Matsuno, T. 2024, *A&A*, 691, A226
- Chen, Y., & Gnedin, O. Y. 2024, arXiv e-prints [arXiv:2401.17420]
- Dalessandro, E., Cadelano, M., Della Croce, A., et al. 2024, *A&A*, 691, A94
- Dalessandro, E., Ferraro, F. R., Bastian, N., et al. 2019, *A&A*, 621, A45
- De Angeli, F., Piotto, G., Cassisi, S., et al. 2005, *AJ*, 130, 116
- del Pino, A., Libralato, M., van der Marel, R. P., et al. 2022, *ApJ*, 933, 76
- Dotter, A., Sarajedini, A., Anderson, J., et al. 2010, *ApJ*, 708, 698
- Foreman-Mackey, D., Hogg, D. W., Lang, D., & Goodman, J. 2013, *PASP*, 125, 306
- Gaia* Collaboration (Vallenari, A., et al.) 2023, *A&A*, 674, A1
- Häberle, M., Neumayer, N., Seth, A., et al. 2024, *Nature*, 631, 285
- Harris, W. E. 1996, *AJ*, 112, 1487
- Horta, D., Schiavon, R. P., Mackereth, J. T., et al. 2020, *MNRAS*, 493, 3363
- Knoetig, M. L. 2014, *ApJ*, 790, 106
- Leaman, R., VandenBerg, D. A., & Mendel, J. T. 2013, *MNRAS*, 436, 122
- Libralato, M., Bellini, A., van der Marel, R. P., et al. 2018, *ApJ*, 861, 99
- Libralato, M., Bellini, A., Vesperini, E., et al. 2022, *ApJ*, 934, 150
- Libralato, M., Bedin, L. R., Griggio, M., et al. 2024, *A&A*, 692, A96
- Marín-Franch, A., Aparicio, A., Piotto, G., et al. 2009, *ApJ*, 694, 1498
- Massari, D., Breddels, M. A., Helmi, A., et al. 2018, *Nat. Astron.*, 2, 156
- Massari, D., Koppelman, H. H., & Helmi, A. 2019, *A&A*, 630, L4
- Massari, D., Helmi, A., Mucciarelli, A., et al. 2020, *A&A*, 633, A36
- Massari, D., Aguado-Agelet, F., Monelli, M., et al. 2023, *A&A*, 680, A20
- Massari, D., Bellazzini, M., Libralato, M., et al. 2025, *The Hubble Missing Globular Cluster Survey. I. Survey overview and the first precise age estimate for ESO452-11 and 2MASS-GC01*
- Mighell, K. J., Rich, R. M., Shara, M., & Fall, S. M. 1996, *AJ*, 111, 2314
- Milone, A. P., Piotto, G., Bedin, L. R., et al. 2012, *A&A*, 540, A16
- Milone, A. P., Marino, A. F., Di Criscienzo, M., et al. 2018, *MNRAS*, 477, 2640
- Monty, S., Belokurov, V., Sanders, J. L., et al. 2024, *MNRAS*, 533, 2420
- Nardiello, D., Libralato, M., Piotto, G., et al. 2018, *MNRAS*, 481, 3382
- Piotto, G., Milone, A. P., Bedin, L. R., et al. 2015, *AJ*, 149, 91
- Recio-Blanco, A. 2018, *A&A*, 620, A194
- Sarajedini, A., Bedin, L. R., Chaboyer, B., et al. 2007, *AJ*, 133, 1658
- Searle, L., & Zinn, R. 1978, *ApJ*, 225, 357
- Sollima, A., Baumgardt, H., & Hilker, M. 2019, *MNRAS*, 485, 1460
- Vasiliev, E., & Baumgardt, H. 2021, *MNRAS*, 505, 5978
- Watkins, L. L., van der Marel, R. P., Libralato, M., et al. 2022, *ApJ*, 936, 154

## Appendix A: Systematic correction

We extensively checked for systematics introduced by GATIAHUB and we found a non-linear correlation between  $\mu_\delta$  and the position of stars in the field of view, in particular with the  $\delta$  coordinate (see Fig. A.1a). Firstly, we cross-checked this relation with the pure *Gaia* DR3 PM and we did not find any significant relation, reinforcing the idea of having introduced a systematic using GATIAHUB. We then choose to use *Gaia* as reference to compensate for this dependence. We corrected the *GH* PM of each star by subtracting the difference between itself and the median value of the *Gaia* PMs of the 25 neighbors stars. With this approach we were able to remove the systematic, obtaining an uncorrelated  $\mu_\delta$  against  $\delta$  (see Fig. A.1b).



(a)



(b)

Fig. A.1: *GH* PMs  $\delta$  component against the sky  $\delta$  coordinate. (a) The uncorrected PMs and (b) after the correction. The gray dashed line shows the median value of the distribution, used as visual reference.